# Visualization of ultrasonic cavitation in visible and IR spectra

A. Osterman[1], O. Coutier-Delgosha[2], M. Hocevar[1] & B. Sirok[1]
[1]*Faculty of Mechanical Engineering, University of Ljubljana, Slovenia*
[2]*Arts et métiers ParisTech, Centre de Lille, France*

## Abstract

Ultrasonic cavitation was generated with ultrasound of 33 kHz in a small closed water tank, containing about one liter of water. Cavitation was experimentally observed simultaneously with high-speed cameras in IR and visible spectra. Cameras were capturing images of the same observation area. From the images obtained time-dependent velocity fields were calculated for both cameras. Velocity calculation was based on pattern and similitude recognition between pairs of consecutive images. Images from the visible spectrum were also processed in order to detect the individual graphical objects presumably linked with cavitation collapses. As a result, correlations between velocity fields from each camera and correlations between velocity fields and cavitation collapses were determined. Strong correlations were found in all cases. Additionally, a delay was found for the velocities from the camera in the visible spectrum when compared to the thermographic results. Also the behavior of the correlation between cavitation collapses and velocities was in some cases found to be dependent on whether the velocities were from the images taken in the visible or the IR spectrum.
*Keywords: cavitation, ultrasound, IR thermography, velocity fields, correlation, bubble collapse, visualization.*

## 1 Introduction

Ultrasonic cavitation has many applications (Mason and Lorimer [1], Brennen [2]) and an obvious question that arises when one is dealing with it, is what is happening inside. In search for a non-trivial answer, an experimental approach to measure basic flow quantities seems appropriate, since currently available

WIT Transactions on Engineering Sciences, Vol 69, © 2010 WIT Press
www.witpress.com, ISSN 1743-3533 (on-line)
doi:10.2495/AFM100391

numerical methods cannot sufficiently handle a phenomenon of such complexity as found in practical use in industrial processes, medicine etc. [3–6], although the experimental approach has also some limitations. As cavitation actually consists of bubble collapses, often very fast sensors are needed. Additionally, it is desirable to use non-intrusive methods to preserve a true cavitating fluid flow (Franc and Michel [7]), such as visualization [8–14].

This paper presents several new approaches to cavitation. First, it describes thermovision method applied to measure cavitation thermal effects. On a scale of a single bubble very high temperatures can occur during the compression stage of cavitation collapse (Rae *et al.* [15], Kim *et al*. [16]) and temperature delay is a known phenomenon during cavitation growth (Brennen [2], Franc and Michel [7]). Also in case of cryogenic liquids local temperature drops are reported (Ishii and Murakami [17]). However, proper experimental measurements of temperatures are very scarce (Dular *et al*. [18]) and few experimental data of that kind are available (Fruman *et al*. [19]).

Secondly, algorithm for determination of velocity fields based on experimental visualization results is presented, so that velocities near solid boundaries in cavitating water are obtained. The algorithm works similarly to PIV (Stanislas *et al*. [20]) but no seeding particles are needed. Thirdly, detection of collapses of cavitating bubbles is presented, which are then identified as a driving factor for measured velocity fields.

Cavitation was generated in an ultrasonic cleaning device, filled with water. For visualization, high-speed cameras that work in IR and visible spectra were used. They were synchronized and were taking images of the same observation area. Detection of collapses of bubbles was based on images from a high-speed camera operating in the visible spectrum. Presented results show that there is good agreement between velocity fields from both cameras and that velocity magnitude is in proportion with the number of cavitation collapses.

## 2 Experimental set-up

Experimental set-up is presented in figure 1. Cavitation was generated in a closed container of an ultrasonic cleaning device, partially filled with water. It was generated with a piezoelectric transducer oscillating at 33 kHz. A vessel containing approx. 1 liter of untreated tap water was just partially filled, then air-tightly closed with a lid, having an acrylic-glass tube (opened just at the bottom end) attached to it. When the tube was inserted in the water so that its open end was below the initial water level, it was possible to raise the water level above the edge of the vessel by evacuating the air through a valve at the top of the tube. On the upper end of the tube an observation window was mounted. Such set-up was necessary to obtain free space for laser sheet illumination needed for visualization in the visible spectrum. Through the observation window two synchronized cameras running at 66 Hz were taking images of the same observation area in sequences of approx. 20 s. A sapphire glass window was chosen because it is transparent in both IR and visible spectra (Edmund Optics [21]), which were the operating ranges for our cameras.

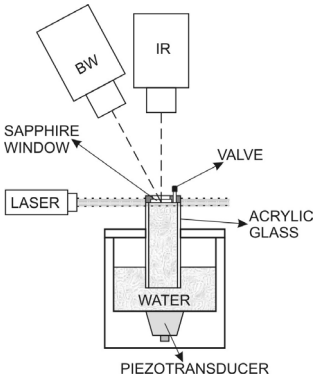


Figure 1: Experimental set-up.

A thermographic camera CMT384SM Thermosensorik, operating in the IR spectrum ranging from 1.5 to 5 μm was used. Resolution was set to 384x288 pixels and exposition time was 1 ms. Temperature fields were taken at the water–sapphire window interface because in the measured spectrum water is not transparent to IR (Hale and Querry [22]). It was checked that 20 μm thick water film was completely opaque for the measured part of the IR radiation. The uncertainty of the mean water operating temperature was ±0.15 K. More important in our case is that the uncertainty of temperature changes in a single point, relative to the operating temperature, was only ±0.03 K.

The camera for visualization in the visible spectrum was Basler Scout scA640-70gm (resolution 640x480 pixels, exposition time 1 ms). Illumination for the camera was provided by a collimated laser Quantum Ventus 520 (527 nm, 700 mW), generating approx. 1 mm thin laser light sheet. It was positioned in parallel with the observation window, with its front and back edges still illuminated.

## 3 Image processing

With both cameras being synchronized, series of images were taken. Thermocamera images (TC) were representing temperature fields, while the camera in visible spectrum took black-and-white images (BW) of particles in the illuminated layer of water. Example of TC and BW images is shown in figure 2.

To obtain further information about the observed cavitation, images were processed in several ways. First, brightness and contrast values of the raw images were modified so that useful information covered the larger part of the 8-bit span of grayscale images. Secondly, velocity fields were calculated. An example of an obtained velocity field is shown in figure 3. Additionally, large objects were detected on BW images. Time series of velocities and frequency of large objects were then filtered. The same filter was used in all instances. On these series correlation was applied to quantify their relationships and interdependence.

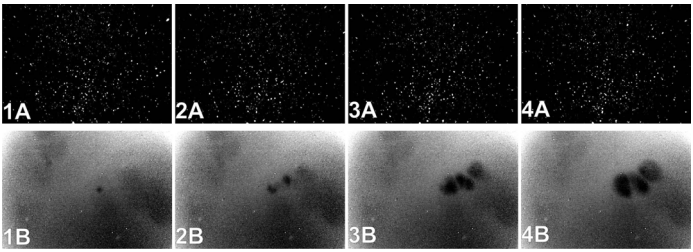


Figure 2: Example of series of BW (A) and TC (B) images (time between frames is 15 ms, frame size is 13x19 mm).

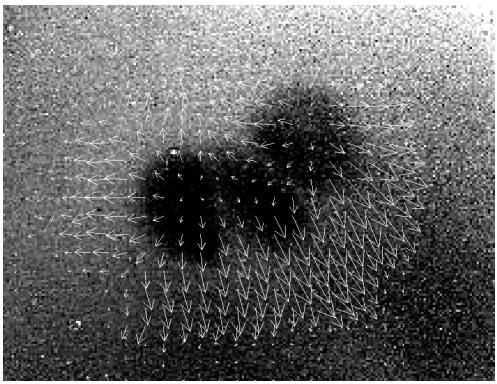

Figure 3: Example of instantaneous velocity field superposed on TC image.

### 3.1 Velocity field calculation

An algorithm for the estimation of displacement and, consequently, velocity was developed. To estimate displacement and velocity from two consecutive images, 2D image cross correlation was applied. All procedures in a selected region of interest were applied in two consecutive images (one pair) in the image sequence. Velocity was calculated from displacement according to camera frame rate and image pixel size.

Measurement uncertainty of PIV measurements is in the range of 1% (Stanislas *et al*. [20]). We estimate that using our algorithm for the velocity measurements the same level of uncertainty is achieved.

#### 3.1.1 Selection of interrogation windows

Velocity estimation was performed in a selected matrix of 34x22 locations in the first image of the chosen pair. A set of interrogation windows of different sizes was extracted from the first image for every selected location.

The best results were obtained for the starting size of interrogation window of 45x45 pixels, reducing to the final size of 35x35 pixels with a step size of 2 pixels. Interrogation window was moved across the second (consecutive) image in both horizontal and vertical direction. A rate of successful searches and

accurate space localization were considered. By defining smaller interrogation windows, not enough details from images were included, producing scattered results. By using larger windows, velocity field was averaged too much and the details of local velocities were lost.

### 3.1.2 Selection of best finds

For each interrogation window size up to 5 locations were found in the second image, ordered by the similarity of the pattern in relation to the pattern of the template of the first image. The similarity was quantified with 2D cross-correlation. The one that was selected had the highest correlation coefficient where the distance from the template was smaller than a selected value of 15 pixels. Additionally, locations were also rejected on the basis of the lowest allowed normalized correlation limit, set to 0.5. A value of 1 corresponded to exactly the same patterns in both templates. These limitations served to prevent that the determination of displacements and velocity vectors would be very different from those of their neighbors.

## 3.2 Large object detection

From observation of BW images the existence of two types of objects was apparent: a vast majority of small moving objects and very few large objects that appeared on only one image and disappeared on another. It was assumed that the first ones show laser light dissipation on microbubbles of undissolved gas and solid impurities while the second ones actually show cavitation bubble collapses. In figure 4 three examples are provided, taking three consecutive images (A, B, C), showing for each example the same observation area through time.

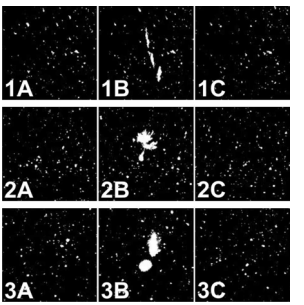


Figure 4: Examples of sequences of consecutive images (A–C) containing collapse structures (B).

It is clearly visible that in B-images some objects are significantly bigger than the others and that they are not present in either A or C images. The actual shapes of these collapse-related objects probably show some parts of bubble splashing against a solid wall (Tong *et al*. [23]) which was in our case the sapphire observation window. Shapes may be more or less deformed circles due to the existing velocity field, pressure gradients, interaction with other bubbles

etc., causing that the microjet is not perpendicular to the window. In some cases several large objects together in the same image may also indicate secondary collapse(s) (Bai *et al*. [24]).

The relationship between the number of detected objects and their area is shown in figure 5. Distributions for a random single image (gray circles) and for the average of the whole sequence (little black squares) are presented, where the number of objects in one image is counted. Note the logarithmic scales that were used because the number of objects so drastically reduces with their increased area. The number of objects that is smaller than unity represents that they are not present on every image. To determine if an object is large several thresholds for object area were used, set from 10 to 50 pixels with a step of 5 pixels. Within this range, the frequency of large objects reduces for approximately a thousand times.

Using the obtained classification of detected objects, the appearance of collapse-related objects in time in a certain region in each BW image was analyzed. This is presented in figure 6. The left image (A) shows the original BW image. From all objects detected in it, only the ones with their area greater than a given threshold were preserved, and are shown in the image (B). The concentric circles around a chosen point define search areas. Radii were increased from 20 to 120 pixels with 20-pixel steps. For each area, the number of included (fully or partially) objects (e.g. objects 1-3) was calculated.

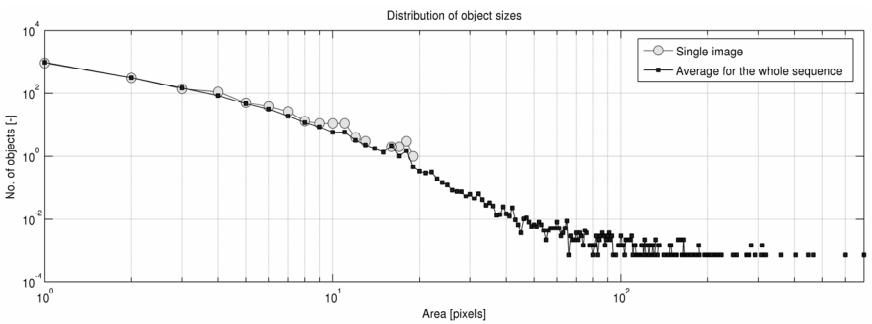


Figure 5: Distribution of frequency of objects with regard to their size.

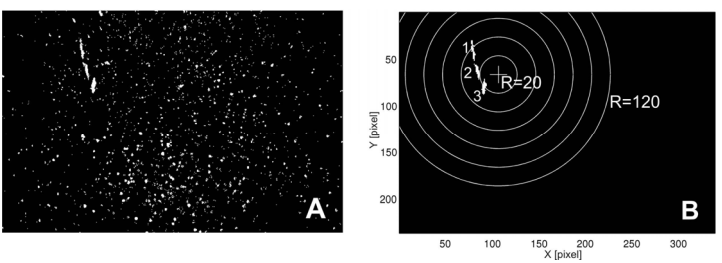


Figure 6: Determination of collapse-related objects (1-3) from original images (A) and their counting inside circular searched areas (B).

In order to continue, time series of these quantities were obtained by computing velocity fields and presence of large objects for each image.

### 3.3 Filtering

Spatial representation of computed velocity magnitudes in one moment in time are presented in figure 7. The left image stands for the velocities from the BW image, whereas the right image is for the velocities from corresponding TC image.

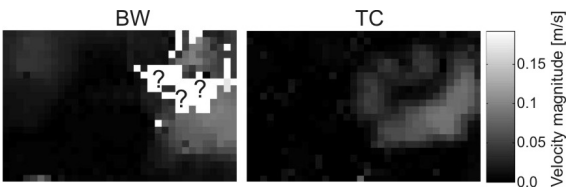


Figure 7: Spatial representation of velocity magnitudes in one moment for both cameras.

When there is insufficient correlation, no velocity in a point is obtained. Generally, in BW series more velocities were missed than in TC series. This is represented in figure 7 where in some areas there are question marks. For computational purposes the velocities in these points were fixed to zero, although they often appeared near the areas with the highest velocities. To compensate this, a low-pass filter (in temporal sense) was applied. A 1st order Butterworth filter was chosen as such filters are monotonic and have maximally flat magnitude response in the passband (Bianchi and Sorrentino [25]). Cutoff

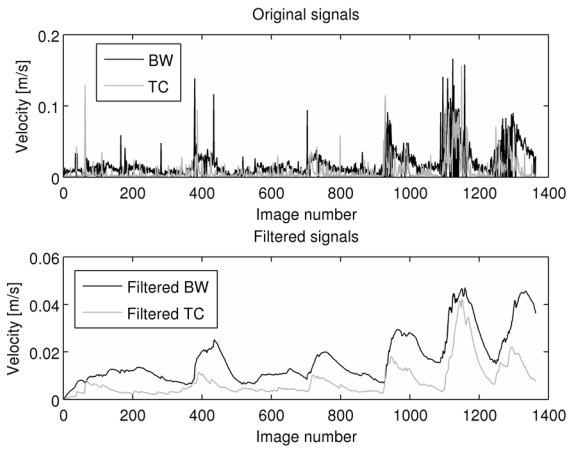


Figure 8: Comparison between original and filtered time series of velocities in a single point.

frequency, for which the magnitude response of the filter was $\sqrt{1/2}$, was set to 0.33 Hz. Original and filtered signals of temporal velocity magnitudes in one point are presented in figure 8.

The same filter was applied to the data concerning the counting of large object appearance. First, the same phase shift was produced, and secondly, the original data were ill-conditioned for comparison with velocity time series because they consisted of sporadic integers. This was greatly improved after the filter was applied.

## 4 Results

Some comparisons between BW and TC velocities were already presented in figure 7 (spatial distribution) and figure 8 (time series). In figure 7, velocities are higher on the right side of each image and have similar magnitudes (where defined), as can be seen from gray levels. In figure 8, velocities in one point are displayed as time series, where time advancement is indicated by image number. General course is the same for both BW and TC, although TC values are smaller. Measured velocities are mostly in order of a few cm/s. The comparison of temporal signals also shows that TC signal slightly precedes BW signal (note the positions of peaks). This is presented in more detail in figure 9, where computed correlations between BW and TC signals are shown.

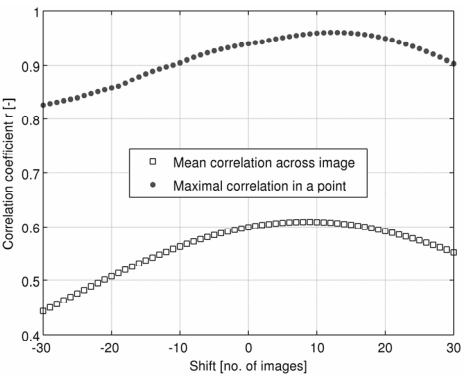


Figure 9: Correlation of velocity signals, shifted in time.

Correlation r was calculated as

$$r = \frac{N\sum XY - \left(\sum X\right)\left(\sum Y\right)}{\sqrt{\left[N\sum X^2 - \left(\sum X\right)^2\right]\left[N\sum Y^2 - \left(\sum Y\right)^2\right]}}, \quad (1)$$

where N is the number of images in a series which is in further analysis the same as the number of data in X or Y, which are vectors of compared quantities (e.g. velocities, number of objects, average brightness etc.) at a chosen position in an image.

While the maximum of the best correlation obtained across the image for a single point is reached when signals are shifted for 13 images (TC delayed for 0.2 s), the maximum for mean correlation (mean from all correlations, not from mean velocity) was for 9-images shifted signals (TC delayed for 0.14 s).

In the next step, velocities were compared to collapses (as related by large objects). In figure 10 normalized velocity courses in a single point together with the normalized number of large objects found around that point are shown. Velocities are chosen for the same point as presented in figure 8. A location of the point is shown with a cross in figure 6 (B). In figure 10 results for the search area of radius 40 pixels are presented, while the minimal object size was set to 20 pixels.

Good general agreement can be observed, especially between TC signal and the number of objects, considering that such different quantities are compared.

The effects of the search area radius and the minimal object size on the correlation between the velocities and the number of objects were investigated and the results are shown in figure 11. Correlation for frequency of large objects compared to BW velocities is shown on the left side and for TC velocities on the right side. While increasing the minimum object area causes the correlation to

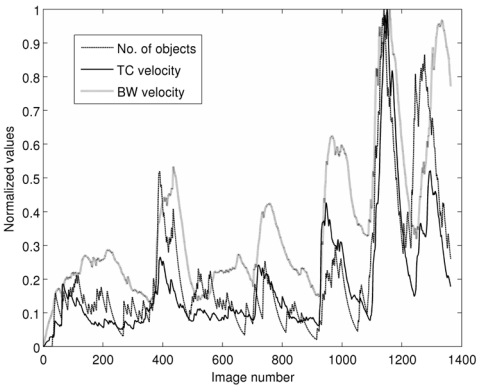


Figure 10: Comparison between velocities and number of objects for time signal in a single point.

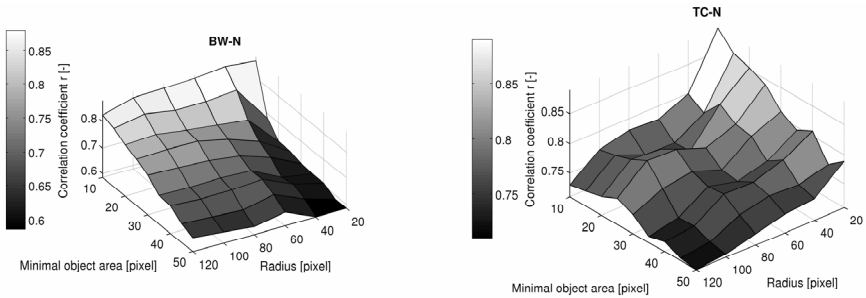


Figure 11: Correlation between velocities and number of objects.

diminish in both cases, the effect of the search area radius is not the same. On the left (BW), the correlation generally grows with increased radius and decreases slowly just for small object areas, while on the right (TC), the correlation decreases with increasing radius of the search area almost over the whole range of values. However, for both cases the best correlation is obtained for the smallest search radius and the smallest minimal object area.

## 5 Discussion

By using a relatively new experimental approach to cavitation (Dular *et al*. [18]), cavitation thermal effects were successfully measured. Temperature drops were in range of a few tenths of kelvin, lasting for a few tenths of a second. Spatial scales were in range of millimeters. Due to physical properties of water which is not transparent in the measured part of IR spectrum, temperatures at the water-observation glass interface were measured.

By taking into account the finite thickness of the observing layer of water illuminated with laser light sheet (BW case) which was thicker than the observed interface between water and sapphire window (TC case), it can be also explained why measured TC velocities were smaller than BW velocities, because further away from the observation window the effect of solid wall due to viscosity gets smaller and velocities are higher.

A short note about the cameras: frames were taken at 66 Hz with 1 ms exposure time. It was estimated that the frame rate of both cameras is sufficiently high. The increased frame rate would not significantly contribute to better results, especially not in TC case, whereas in BW case it is expected that in the critical moments around collapses, velocities could be found more often. The real advantage of higher frame rate is in better detection and observation of collapses themselves (BW images), where additional information on collapse shape may be useful for prediction of velocity field orientation or direction of thermal effect spreading etc.

As untreated tap water was used, many of very small objects were related to light reflections on undissolved gas bubbles and on other particles, not connected with cavitation. It is believed that by using filtered and degassed water many of these small objects would disappear. While this provides better initial images for large object detection and quantification, it would be a great drawback for velocity field calculation because the searching algorithm would lack handles for detecting similar patterns.

## 6 Conclusions

Experimental investigation of cavitation, generated in an ultrasonic cleaning device at 33 kHz was done based on visualization with two synchronized high-speed cameras, operating in visible and IR spectra, and was further supported with image processing tools. An algorithm was developed to determine temporal velocity fields from visualization images on the basis of similarity searching. Another tool was used to determine individual objects in the images from camera

recordings in visible spectrum. Detected objects were depending on their sizes, connected with cavitation collapses, and several comparisons between velocity fields from both cameras and frequency of collapses were done, quantified by correlation.

The main findings are listed below:

1) Measured velocities resulting from ultrasonic cavitation were in a range of a few cm/s. Similar values were obtained from the analysis of visible and IR images, but velocities were generally higher in the first case.
2) Good agreement between spatial and temporal distributions of velocities was obtained from the analysis of visible and IR images, where for the time series from visible images, velocity information was delayed for about 0.14 s.
3) Cavitation thermal effects were successfully measured, although usually neglected, and were proved useful for cavitation analysis. They were measured in the form of time dependent temperature fields, displaying temperature drops in range of a few tenths of kelvin, lasting for a few tenths of a second and with characteristic lengths in range of millimeters.
4) From the images in visible spectrum individual objects were identified and connection between large objects and cavitation collapses was made. From distribution of object sizes it was determined that large objects occur very seldom, e.g. the smallest appear approx. million times more frequently than the greatest, while the ratio of their sizes is in a range of one to hundred.
5) Good agreement between presence of large objects and velocity magnitude was found, from which a conclusion was drawn that cavitation collapses are driving measured stirring of water. The obtained correlation was higher when frequency of large objects was compared with velocities from IR images.

## References

[1] Mason, T. J. & Lorimer, J. P., *Applied Sonochemistry*: Wiley-VCH, 2002.
[2] Brennen, C. E., *Cavitation and Bubble Dynamics*: Oxford University Press, 1995.
[3] Bretz, N. *et al*, Numerical simulation of ultrasonic waves in cavitating fluids with special consideration of ultrasonic cleaning. *Proc. of IEEE Ultrason. Symp.,* pp. 703–706, 2005.
[4] Servant, G. *et al*, Numerical simulation of cavitation bubble dynamics induced by ultrasound waves in a high frequency reactor. *Ultrason. Sonochem.,* **7**, pp. 217–227, 2000.
[5] Yasui, K. *et al*, FEM calculation of an acoustic field in a sonochemical reactor. *Ultrason. Sonochem.,* **14 (5)**, pp. 605–614, 2007.
[6] Osterman, A., Dular, M. & Širok, B., Numerical Simulation of a near-wall bubble collapse in an ultrasonic field. *J. of Fluid Science and Technology,* **4 (1)**, pp. 210–221, 2009.

[7] Franc, J.-P. & Michel, J.-M., *Fundamentals of cavitation*: Kluwer Academic Publishers, Netherlands, 2004.
[8] Dähnke, S., Swamy, K.M. & Keil, F.J., A comparative study on the modeling of sound pressure field distributions in a sonoreactor with experimental investigation. *Ultrason. Sonochem.,* **6**, pp. 221–226, 1999.
[9] Price, G.J., Harris, N.K. & Stewart, A.J., Direct observation of cavitation fields at 23 and 515 kHz. *Ultrason. Sonochem.,* **17 (1)**, pp. 30–33, 2010.
[10] Leighton, T.G., Bubble population phenomena in acoustic cavitation. *Ultrason. Sonochem.,* **2 (2)**, pp. 123–136, 1995.
[11] Moussatov, A., Granger, C. & Dubus, B., Cone-like bubble formation in ultrasonic cavitation field. *Ultrason. Sonochem.,* **10**, pp. 191–195, 2003.
[12] Birkin, P.R., Delaplace, C.L. & Bowen, C.R., Electrochemical and photographic detection of cavitation phenomena within a variable frequency acoustic field. *J. Phys. Chem. B,* **102**, pp. 10885–10893, 1998.
[13] Chen, H. *et al*, High-speed observation of cavitation bubble cloud structures in the focal region of a 1.2 MHz high-intensity focused ultrasound transducer. *Ultrason. Sonochem.,* **14**, pp. 291–297, 2007.
[14] Chen, H., Li, X. & Wan, M., The inception of cavitation bubble clouds induced by high-intensity focused ultrasound. *Ultrasonics,* **44**, pp. e427–e429, 2006.
[15] Rae, J. *et al*, Estimation of ultrasound induced cavitation bubble temperatures in aqueous solutions. *Ultrason. Sonochem.,* **12**, pp. 325–329, 2005.
[16] Kim, K.Y., Byun, K.-T. & Kwak, H.-Y., Temperature and pressure fields due to collapsing bubble under ultrasound. *Chem. Eng. J.,* **132**, pp. 125–135, 2007.
[17] Ishii, T. & Murakami, M., Comparison of cavitating flows in He I and He II. *Cryogenics,* **43**, pp. 507–514, 2003.
[18] Dular, M. *et al*, Local thermal effects of ultrasound induced cavitation. *Proc. of 6th Int. Symp. on Cavitation CAV2006,* 2006.
[19] Fruman, D.H., Reboud, J.L. & Stutz, B., Estimation of thermal effects in cavitation of thermosensible liquids. *Int. J. of Heat Mass Transf.,* **42**, pp. 3195-3204, 1999.
[20] Stanislas, M. *et al*, Main results of the second international PIV challenge. *Exp. Fluids,* **39**, pp. 170–191, 2005.
[21] Edmund Optics, Sapphire windows technical images, http://www.edmundoptics.com
[22] Hale, G. M. & Querry, M. R., Optical constants of water in the 200 nm to 200 μm wavelength region". *Appl. Opt.,* **12**, pp. 555–563, 1973.
[23] Tong, R.P. *et al*, The role of 'splashing' in the collapse of a laser-generated cavity near a rigid boundary. *J. Fluid Mech.,* **380**, pp. 339–361, (1999).
[24] Bai, L. *et al*, A high-speed photographic study of ultrasonic cavitation near rigid boundary. *J. of Hydrodynamics,* **20 (5)**, pp. 637–644, 2008.
[25] Bianchi, G. & Sorrentino, R., *Electronic filter simulation and design*: McGraw-Hill, 2007.